

2

Ewart, T.E., and S.A. Reynolds, Ocean acoustic propagation measurements and waves in random media, in Tatarskii, V.I., A. Ishimaru and V.U. Zavorotny, eds., Wave Propagation in Random Media (Scintillation), SPIE Press, PM09, April, 1993.

Ocean acoustic propagation measurements and wave propagation in random media

Terry E. Ewart and Stephen A. Reynolds

Applied Physics Laboratory, University of Washington, Mailstop HN-10, Seattle, Washington, 98105

ABSTRACT

Over the last two decades, observations of acoustic scintillations in the ocean have been useful in testing theories that predict the statistics for WPRM. Ocean acoustic observations differ from scattering processes observed in other WPRM sub-fields in two important ways. First, the statistics of the refractive index can be determined accurately from oceanographic measurements. Hence, exacting tests of theories can be done when careful measurements of the medium and the wavefield are made synoptically. Second, the scattering of acoustic energy is predominantly influenced by the ocean internal wave field, which tends to exhibit statistical stationarity in many ocean regimes, and not by non-stationary turbulent processes, as observed in the atmosphere. We discuss space/time acoustic propagation experiments carried out in three scattering regimes: (1) weak, where the Rytov approximation is valid; (2) moderate, where multiple scattering theory is required; and (3) the case where multiple scattering in a single medium irregularity is encountered. A review is presented of the measurements and comparisons with theory.

It is clear from field and numerical experiments that 2-point statistics cannot possibly explain the observations of intensity. Because two-point statistics are the norm when interpreting both medium and wavefield measurements, the possible failure of Gaussian statistics must be addressed. This has yet to be done. We will discuss remaining issues for which we believe further study is needed.

2. INTRODUCTION

This conference addresses fluctuations in the propagation of waves in media with random index of refraction fields. This discipline is rooted in the practicalities of dealing with those fluctuations, and the beauty associated with explaining them. We present observations of acoustic scintillation statistics measured by our group over three paths in the deep ocean. The ocean environment is ideal in the sense that the scattering refractive index field may be monitored simultaneously with scintillation measurements. However, ocean paths are complicated by an anisotropic scattering field and a depth-dependent sound speed and scattering strength. The experiments we describe attempted to minimize these complications by using propagation ranges less than 20 km. In particular, the second path we discuss was nearly horizontal. Evaluations of 4th moment theory have successfully predicted the strong ($\langle I^2 \rangle > 2$) scintillation levels from this path.

The complex amplitudes of the fluctuations are observed to have highly non-Gaussian behavior; hence we are "stuck" with a need to understand the phenomena at complexities beyond the usual two-point statistics. Numerical simulations are ideal for studying field statistics over a broad range of scattering conditions. The latter part of our presentation

DTIC
ELECTE
FEB 25 1994

A

This document has been approved
for public release and sale; its
distribution is unlimited.

AD-A276 165

94-05758



94 2 23 007

DTIC QUALITY INSPECTED 1

**Best
Available
Copy**

discusses parabolic equation-based numerical experiments used to study intensity probability distributions. Using our ocean acoustic measurements as a starting point, we use the generalized gamma distribution to model simulated data from weak and through strong scatter to saturation.

Since the introduction of the system of parabolic moment equations by Shishov¹ (1968), we have had the tantalizing expectation of understanding the scattering physics. It has been a long road and we highlight some of the work pertinent to the experiments presented. We would like to emphasize that understanding observations of ocean acoustic scintillation has driven the development of theory.

Using the Garrett and Munk² (1972) ocean internal wave model, Uscinski³ (1980) applied 4th moment theory to the published⁴ 1971 Cobb Seamount experiment temporal spectra of intensity. These were only partial solutions however, and in 1982 Uscinski⁵ provided the first full range solution to the 4th moment equation for a plane wave initial condition. Uscinski et al.⁶ and Ewart et al.⁷ gave predictions for the Cobb experiment intensity time spectra that showed the proper acoustic frequency dependence. The scintillation index remained under-predicted. That theory included a point source initial condition. Macaskill⁸ (1983) provided a correction term to the 4th moment using two-scale expansions. That theory was applied by Macaskill and Ewart⁹ (1984) to "numerical experiments" based on parabolic wave field-marching through computer-generated index of refraction fields. There was good agreement between the full range theory with the correction term, and the simulated data intensity correlations for low values of the scattering parameters (for Gaussian and 4th order power law medium transverse spectra). Ewart and Reynolds¹⁰ (1984) presented the initial results from a subset of the MATE (Mid-Ocean Acoustic Transmission Experiment) experiment data compared to zeroth order theory using an ocean model that included linear ocean internal waves and a refinement termed finestructure. Agreement between the theory and intensity correlations from the data improved, but the under-prediction remained. Ewart et al.¹¹ (1985) showed that the cross frequency 4th moment theory of Uscinski and Macaskill¹² (1985) severely under-predicted the cross-spectra for intensity records at differing frequencies. A full range solution to the 4th moment equation using the path integral was formulated by Uscinski et al.¹³ (1986). Earlier path integral solutions were asymptotic to short and long range cases, and not applicable to the experiments at Cobb Seamount. In this paper, we include linear internal waves and finestructure as well as a correction term to the theory for the MATE predictions.

Macaskill and Ewart¹⁴ (1984) provided a model of the intensity moments and an intensity probability distribution of the log intensity that predicted several experiments spanning a wide range of scattering parameters. Ewart and Percival¹⁵ (1986) demonstrated that the generalized gamma distribution models both field and numerical experiment data (acceptance at the 90% confidence level). Using numerical experiments, Ewart¹⁶ (1989) demonstrated (for 8 decades in scattering strength corresponding to 3 decades in wavenumber and 6 decades in range) that the generalized gamma distribution is a valid model for the intensity probability distribution for WPRM. In the past few years, Uscinski's Cambridge Group has produced several publications on comparisons of wavefield simulations with numerical solutions for the 4th moment equation. References

✓
□
□
A234258

Availability Codes	
Dist	Avail and/or Special
A-1	

are found in Leonard and Uscinski¹⁷. Recently, Martin and Flatte^{18, 19} extended these simulation techniques to 3-D media for a point source.

Almost all of the testing problems arise when theories are confronted with real data sets. Having full range solutions for many of the possible 2-point separations requires comparisons with observations for validation; that is the crux of this paper.

2.1. Experiments at Cobb Seamount

Ewart⁴ examined ocean acoustic fluctuations, where both the phase and the amplitude (4 and 8 kHz transmissions over an 18 km path using fixed sources and receivers) were recorded synoptically (6 days) with oceanographic measurements. The observed intensity fluctuations were large ($\langle I^2 \rangle > 2$). The available theories (many based on the Rytov approximation) were able to predict the phase fluctuations (Desaubies^{20, 21, 22} and Munk and Zachariassen²³). However, these same theories were hopelessly inadequate for predicting the large intensity variance, or its spectral decomposition. For that experiment, the oceanographic observations were insufficient to determine the full 3-space/time ocean model.

In a second experiment at Cobb Seamount (MATE), the frequencies were expanded to include 2 and 13 kHz. The space/time medium fluctuations along the transmission path region were sampled by many different sensors so that various projections of the 3-space/time statistics were known. Twelve days of data on a downward path and two days on an upward path were recorded (the paths were both totally refracted). As in the first experiment, the fixed source and receivers allowed determination of the travel time to within a few microseconds, and it was possible to separate the upward or downward arrivals into identifiable Fermat paths^{24, 25, 26}. In this paper, we will only discuss the MATE results.

2.2. The AIWEX Acoustic Transmission Experiment (AATE)

AATE was conducted from a multi-year icefield north of Prudhoe Bay, Alaska (Ewart and Reynolds²⁷). Transmissions at 2, 4, 8, and 16 kHz were made over a 6.4 km path for 12 days to a receiving array with a 153 m vertical (synthetic) aperture. As in MATE, the arrivals were isolated into single Fermat paths and the phase and amplitude results were obtained. In AATE the intensity fluctuations were very weak, and the oceanography (as determined synoptically by the Arctic Internal Wave Experiment (AIWEX) investigators) was highly non-stationary, even when viewed over the operation's short duration.

Testing the full range moment equation theories has evolved into more precise evaluations of theories and subtle increases in our understanding of ocean variability. It is our contention that the remaining tasks facing us in our quest to validate the theories will boil down to "getting the medium right," rather than any order one changes in the theories. In the atmosphere, investigators have had to contend with a severe lack of stationarity in turbulent processes. In the ocean, horizontal homogeneity and stationarity of processes are good assumptions, but the actual spectral models are complex in both wavenumber and frequency.

3. OCEAN INDEX OF REFRACTION VARIABILITY

In the late 1960's and early 1970's, it was recognized by oceanographers that submesoscale variability was dominated by the processes of internal waves - dynamic oscillations on the weak internal density gradients of the ocean. In a series of papers, Garrett and Munk^{2, 28} outlined a model for the linear internal wave field of the ocean. These dynamics differ from turbulence in that they are anisotropic, and the dispersion relation requires inclusion of spatial/temporal coupling. Another complication is additional variance in the index of refraction from processes that have been termed *finestructure*²⁹. Finestructure may represent a significant fraction of the total $\langle n^2 \rangle$, and cannot in general, be ignored. Unlike the atmospheric case, internal wave velocities produce a much smaller effect on the index of refraction (as seen by a propagating wave) than do internal wave vertical displacements. To set the stage for introducing the distinctions between atmospheric turbulence and ocean variability, we present Figure 1.

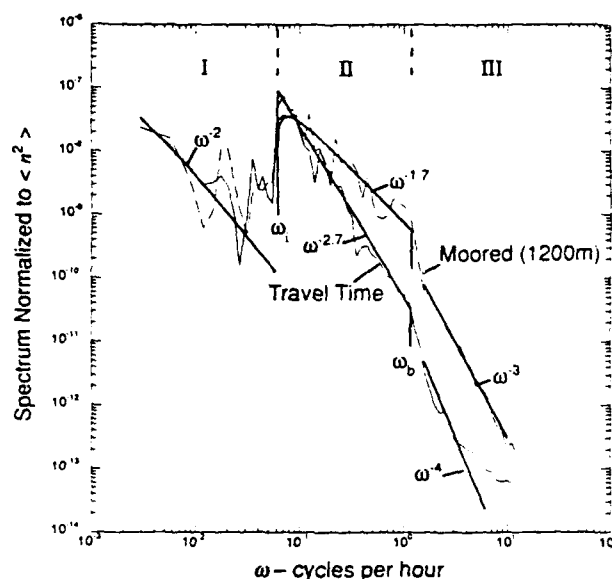


Figure 1. MATE phase and moored temperature sensor data converted to $\langle n^2 \rangle$ units. (Note that cyclical units are used in the Figures.)

Here we have plotted the 2 kHz travel time spectrum of the MATE experiment, in $\langle n^2 \rangle$ units. The same normalization has been done for one of the moored (fixed point) temperature spectra in the experiment, where the temperature fluctuations measured in the mooring have been converted to index of refraction fluctuations. The integrals of both spectra equal $\langle n^2 \rangle$. The frequencies between the inertial frequency, ω_i , and the buoyancy frequency, ω_b , Regime II, is the band where linear internal wave dynamics is allowed. Regime I below ω_i , that extends (unobservable in the spectrum) into Region II, is the finestructure regime, and Regime III above ω_b , is the high-vertical-wavenumber microstructure with a very small total energy. In both spectra, the energy in the tide lines

has been removed by combined modeling of stochastic and deterministic processes. The moored spectrum of the index of refraction is

$$\Phi_M(\omega) = \int_{-\infty}^{\infty} \int_{-\infty}^{\infty} \int_{-\infty}^{\infty} \Phi_n(\kappa_x, \kappa_y, \kappa_z, \omega) d\kappa_x d\kappa_y d\kappa_z, \quad (1)$$

where Φ_n is the 3-space/time spectrum of n . We need the medium correlation function projected (integrated) in the propagation direction, $B_{P,n}$. For straight ray propagation in z ,

$$B_{P,n}(\nu_x, \nu_y, \tau) = \int_{-\infty}^{\infty} \int_{-\infty}^{\infty} \int_{-\infty}^{\infty} \Phi_n(\kappa_x, \kappa_y, \kappa_z = 0, \omega) e^{i(\kappa_x \nu_x + \kappa_y \nu_y + \omega \tau)} d\kappa_x d\kappa_y d\omega, \quad (2)$$

where $(\kappa_x, \kappa_y, \kappa_z, \omega)$ and $(\nu_x, \nu_y, \nu_z, \tau)$ are the spectral and separation coordinates respectively. The spectrum of the phase, S , is

$$\Phi_S(\omega) = k^2 z_R \int_{-\infty}^{\infty} B_{P,n}(0, 0, \tau) e^{-i\omega \tau} d\tau. \quad (3)$$

$B_{P,n}(0, 0, 0) = \langle n^2 \rangle L_P$, with L_P the integral scale from the integration in range, k is the acoustic wavenumber, and z_R is the range. The projected medium correlation function, $B_{P,n}(\nu_x, \nu_y, \tau)$, is usually called the Transverse Correlation Function, TCF. It is analogous to the integrated structure function in atmospheric scattering literature. This expression has been generalized to the curved ray case by Esswein and Flatté³⁰.

For normalization, we use the standard parameters of the parabolic moment equations, where two parameters, scattering strength, Γ , and the scaled range Z , represent the scattering regimes,

$$\Gamma = k^3 \langle n^2 \rangle L_P L_y^2, \quad Z = \frac{z_R}{k L_y^2}, \text{ and } \langle S^2 \rangle = \Gamma Z. \quad (4)$$

L_y is the transverse correlation length. In physical terms, Γ is the "Fresnel" distance, $k L_y^2$, divided by the scattering (or coherence) length $(k^2 \langle n^2 \rangle L_P)^{-1}$; Z is the propagation distance scaled by the "Fresnel" distance. Thus, the phase spectrum can be written

$$\Phi_S(\omega) = \Gamma Z \frac{\int_{-\infty}^{\infty} B_{P,n}(0, 0, \tau) e^{-i\omega \tau} d\tau}{B_{P,n}(0, 0, 0)}.$$

We will require more detail on the TCF later in the discussion. The theoretical phase fluctuation and moored spectra plotted in Figure 1 were obtained from the MATE

spectral model and (1) and (3). The steepening of the travel time spectrum in the internal wave regime arises from the dispersion relation; an extra power is subtracted in the negative power law exponent, thus effectively demonstrating the accuracy and applicability of the linear internal wave dispersion relation. In the observable finestructure regime i.e., below ω_i , the spectra are statistically the same, indicating the lack of a dispersion relation. We believe that in the microstructure regime, small scale structures are advected by the internal waves and the power law exponent changes in the same fashion between the spectrum of n and the spectrum of S .

For propagation studies in the turbulence spectrum of the atmosphere as found in Ishimaru³¹, the TCF of the medium is obtained from an assumed spectrum of turbulence that is advected past the measurement apparatus. The TCF for the case of a spectrum, $\Phi_n(\kappa_x, \kappa_y, \kappa_z)$ is

$$\begin{aligned} B_{P,n(turb)}(v_x, v_y, \tau) &= \int_{-\infty}^{\infty} \int_{-\infty}^{\infty} \Phi_n(\kappa_x, \kappa_y, 0) e^{i[\kappa_x(v_x - v_x\tau) + \kappa_y(v_y - v_y\tau)]} d\kappa_x d\kappa_y \\ &= B_{P,n(turb)}[(v_x - v_x\tau), (v_y - v_y\tau)], \end{aligned}$$

where v_x and v_y are the medium velocities transverse to the propagation. The fluctuations in time are the same as the fluctuations at a field point. For such a medium, Φ_S and Φ_M in Figure 1 would have the same spectral dependence. If the internal wave spectrum of the atmosphere plays a role in the scattering of electromagnetic waves, the effects could be detectable from the usual Taylor hypothesis models by precise measurements of the phase and the one-point index of refraction fluctuations for electromagnetic or acoustic propagation.

We turn our attention to reviewing the specific TCF's we will need in discussing ocean experimental results.

3.1. The AATE TCF

As mentioned in the introduction, the AATE propagation geometry sampled a weak scattering environment. Fluctuations in the refractive index were dominated by internal waves. Levine³² showed that the observed environmental variability could be described by a modified GM internal wave model. The internal wave displacement variance was reduced by about a factor of 50 from open ocean values and spectral frequency dependence and modal bandwidth differed from the traditional model. For our purposes, we decompose the vertical variability denoted by mode number, j .

Using the GM formulation, the refractive index spectrum decomposed in terms of frequency and vertical mode number can be written

$$\Phi_n(\omega, j; y) = \langle n^2(y) \rangle G(\omega) H_j, \text{ where} \quad (5)$$

$$G(\omega) = G_0 \frac{(\omega^2 - \omega_i^2)^{1/2}}{\omega^p}, H_j = \frac{H_0}{j^2 + j_*^2}.$$

G_0 and H_0 are normalization constants such that

$$G_0^{-1} = \int_{\omega_i}^{\omega_b} \frac{(\omega^2 - \omega_i^2)^{1/2}}{\omega^p} d\omega, \text{ and } H_0^{-1} = \sum_{j=1}^{\infty} \frac{1}{j^2 + j_*^2}.$$

The level of refractive index fluctuations is related to the internal wave displacement variance, $\langle \zeta^2 \rangle$, by the relative gradient in potential sound speed. That is,

$$\langle n^2(y) \rangle = \left(\frac{1}{c_0} \frac{dc_p}{dy} \right)^2 \langle \zeta^2(y) \rangle. \quad (6)$$

The displacement variance is related in turn to the vertical profile of the internal wave buoyancy frequency. From the environmental observations, $p = 2.2$ and $j_* = 30$ for the AATE site; see Levine³² for details. In general, because $\langle n^2 \rangle$ is a function of depth, scattering is vertically inhomogeneous along ocean rays. This was the case during AATE, and the TCF must be written as a weighted integral of (5) along the ray. We defer further discussion to the section on acoustic results.

3.2. The MATE TCF

Two ray paths were monitored along the MATE 18 km range. Unlike AATE, an effectively homogeneous scattering environment was traversed by the upward ray. However, fluctuations in the refractive index were complicated by the presence of finestructure variability roughly equal in variance to that described by the internal wave model, but apparently having a much longer time scale. This knowledge was obtained using the extensive environmental measurements made during the experiment³³. Because only the downward path was monitored for environmental fluctuations, we predict internal wave variability along the upward path using the GM-model and test the result with the phase spectrum.

Along the MATE paths, the spectrum of the refractive index is modeled as the sum of internal wave and finestructure components

$$\Phi_n = \Phi_{n,IW} + \Phi_{n,FS}. \quad (7)$$

The covariance function of n , B_n , is defined in terms of the internal wave and finestructure correlation functions, and

$$B_n(v_x, v_y, v_z, \tau) = \langle n_{IW}^2(y) \rangle \rho_n, \text{ where } \rho_n = (\rho_{n,IW} + b \rho_{n,FS}). \quad (8)$$

For the downward path, $b = 1$ from observation; for the upward path we assume $b = 0$.

As mentioned earlier, we require the correlation function (8) projected along the direction of propagation. We denote this correlation function as ρ_P . For internal waves (see Equation 12 of Uscinski³), $\rho_{P,IW}(\nu_x, \nu_y, \tau) =$

$$2 \int_{\omega_i}^{\omega_b(y)} G(\omega) \cdot \frac{(\omega_b^2 - \omega^2)^{1/2}}{(\omega^2 - \omega_i^2)^{1/2}} \int_{\kappa_{yc}}^{\infty} \frac{H(\kappa_y)}{\kappa_y} \cos(\alpha \nu_x) \cos(\kappa_y \nu_y) \cos(\omega \tau) d\kappa_y d\omega. \quad (9)$$

$G(\omega)$ is given in (5). Because the buoyancy frequency varies slowly with depth, a WKBJ approximation is used²¹. The modal decomposition used in the AATE case, can now be written in terms of a vertical wavenumber, κ_y :

$$H(\kappa_y) = H_0^{-1} \kappa_{y*} (\kappa_{y*}^2 - \kappa_y^2)^{-1}; \quad H_0 = \int_{\kappa_{yc}}^{\infty} \frac{\kappa_{y*} d\kappa_y}{(\kappa_{y*}^2 + \kappa_y^2)}; \quad (10)$$

$$\kappa_{y*} = t(\omega_b^2 - \omega^2)^{1/2}, \quad t = \frac{\pi j_*}{\omega_0 Y_0}, \text{ and } \kappa_{yc} = \frac{\kappa_{y*}}{j_*},$$

where $\omega_0 = \omega_b(0)$ and Y_0 is the scale depth of $\omega_b(y)$. The internal wave dispersion relationship,

$$\alpha^2 = \kappa_y^2 \frac{(\omega^2 - \omega_f^2)}{(\omega_b^2 - \omega^2)} \quad (11)$$

is used in evaluating (9). The local measurements found that $p = 2.7$ and $t = 3.1 \text{ m}^{-1} \text{ s}$ ($j_* = 6$). For details on the environmental modeling see Levine et al.³³.

The finestructure correlation function is modeled as

$$\rho_{n,FS}(\nu_x, \nu_y, \nu_z, \tau) = e^{\left[-\sqrt{(\nu_x^2 + \nu_z^2) / L_H'^2 + \nu_y^2 / L_V'^2} \right]} e^{(-|\tau| / \tau_0)}. \quad (12)$$

Note that horizontal isotropy is assumed for both internal wave and finestructure fields and is well supported by the measurements. Projecting along the range direction gives for finestructure:

$$\rho_{P,FS}(\nu_x, \nu_y, \tau) = 2L_H' \cdot a \cdot K_1(a) e^{(-|\tau| / \tau_0)}. \quad (13)$$

K_1 is the modified Bessel function and $a^2 = (\nu_x^2 / L_H'^2 + \nu_y^2 / L_V'^2)$.

To first order, the finestructure correlation lengths equal those for internal waves. $L_p = \rho_{P,FW}(0, 0, 0)$, then

$$2L'_H = L_p; L'_V = L_V, \quad (14)$$

where $L_V = 1 / \kappa_y$. Estimating τ_0 is difficult because the experiment did not last long enough; we take $\tau_0 = 500$ h.

Combining internal wave and finestructure terms, the MATE projected covariance function is

$$B_{P,n}(v_x, v_y, \tau) = \langle n_{FW}^2 \rangle \left[\rho_{P,FW}(v_x, v_y, \tau) + \frac{b}{L_p} \cdot \rho_{P,FS}(v_x, v_y, \tau) \right]. \quad (15)$$

4. THE ACOUSTIC EXPERIMENT RESULTS

In this section we review acoustic experiment results. Predictions for the acoustic observations use the TCF's from the previous sections.

4.1. AATE

AATE provides a good example of the complications that can arise from the ocean sound channel. The sound speed profile, along with the deepest and shallowest ray paths for each receiving channel, are shown in Figure 2. There were no deterministic interfering multipaths. The predicted internal wave induced variability in the refractive index, $\langle n^2(y) \rangle$, is also shown.

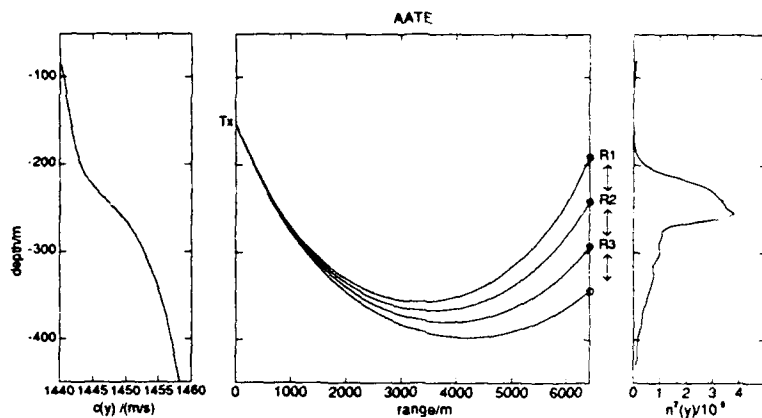


Figure 2. The AATE propagation environment. Locations of the transmitter and three depth cycling receivers are noted on the center ray trace. The rays are traced to the top and bottom positions of the depth cycling (synthetic aperture) array for each receiving channel.

Along ocean rays, the dominant scattering occurs near the turning points. Because of the very weak levels of $\langle n^2 \rangle$ at the ray turning points, the fluctuations observed are very low. The measured variances in the log-amplitudes for four acoustic frequencies, as a function of depth, are shown in Figure 3. For the observed scintillation levels, weak scattering theory is appropriate. We utilize the Rytov approximation-based theory of Munk and Zachariasen²³. The GM-formulation in (4) with parameters determined by the environmental measurements provides the spectrum of $\langle n^2(y) \rangle$ required by theory.

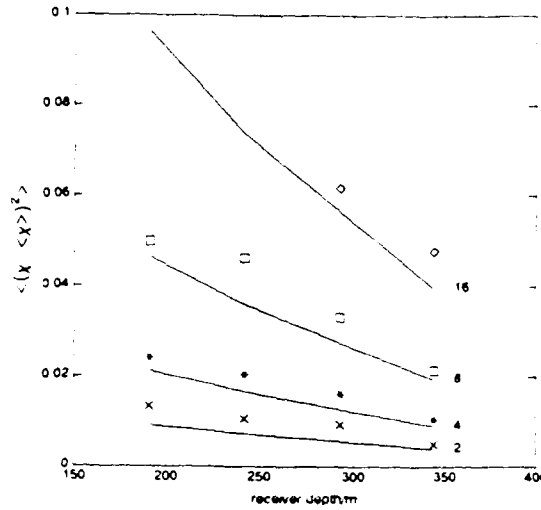


Figure 3. Predicted and observed log-amplitude variance for the receiving array depths. The predictions (solid lines) were obtained by integrating (16). The 2, 4, 8 and 16 kHz observations are shown as crosses, asterisks, boxes and diamonds respectively. (Noise estimates were subtracted from the 16 kHz variances, and are available from the bottom channel only.)

The prediction for the frequency spectrum of phase, Φ_S , and log-amplitude, Φ_χ , for a ray path with a single lower turning point can be written²³

$$\Phi_{S/\chi}(\omega; y) = \sum_{j=1}^{\infty} \frac{k^2 \omega_0 Y_0}{\pi} \int_0^{z_R} dz \sec^2 \theta \left[1 \pm \cos(\beta_{SL} j^2) \right] \frac{\Phi_n(\omega, j; z)}{j(\omega^2 - \omega_L^2)^{1/2}}, \quad (16)$$

$$\text{where } \omega_L^2 = \omega_i^2 + \omega_b^2(y) \tan^2 \theta; \quad \beta_{SL} = \frac{(\pi \omega_b(y))^2}{(\omega_0 Y_0)^2} \frac{z(z_R - z)}{k z_R},$$

and k is the acoustic wavenumber (taken constant). In the terms in brackets in (16), + corresponds to S and - corresponds to χ . ω_0 and Y_0 are scales associated with the

buoyancy frequency $\omega_b(y)$, ω_i is the local inertial frequency, and θ is the ray angle. The integral is carried out along the ray path to range z_R .

To obtain the total variance of χ as a function of depth, Φ_χ in (16) is integrated over $[\omega_i, \omega_b]$. The predictions are shown in Figure 3 for the four acoustic frequencies at AATE. The symbols are the $\langle \chi^2 \rangle$ observations as noted in the caption. For a given depth, observations match the predicted proportional scaling with acoustic frequency. The depth dependence is similar as well. The observations uniformly exceed the predicted values, due to variability outside the internal wave bandwidth.

A better test of theory is provided by the observed frequency spectra. These are shown in Figure 4 for the 8 kHz case at the 191 m receiver. The phase spectrum peaks near ω_i because of mooring motion. (Phase and travel time are equivalent.) Although the total $\langle \chi^2 \rangle$ in Figure 3 exceeds the predicted value, within the internal wave band there is agreement within a factor of 2. The curves denoted GM in the figure are the predictions obtained using the traditional open ocean internal wave values. The observed spectral dependence is better matched by the AIWEX prediction of $\omega^{-2.2}$ than the ω^{-3} dependence of GM. Clearly, our ability to make reasonable predictions was possible only with the local environmental results. At low frequencies, the effect of array motion is apparent in the travel time. (This motion was on the order of 10^{-6} of the 6.4 km path.)

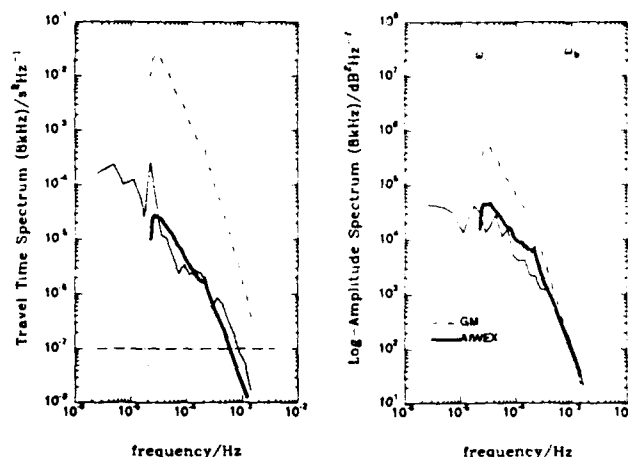


Figure 4. Observed travel time and log-amplitude spectra (solid) compared with predictions¹⁷. The "GM" predictions (light dashed) use open ocean parameters, whereas the AIWEX curves (bold) use the AIWEX model parameters. ω_i and ω_b are noted on the right hand graph. (The departures from regularity in the theory curves are due to the input $\langle n^2(y) \rangle$ profile.) 90% confidence intervals, obtained by numerical simulation, are shown dotted about the 10^{-7} line on the left hand graph.

The two-point spatial covariances are shown in Figure 5. We have estimated the spatial covariance using the top receiver position as a common point and pairing with a series at the noted vertical distance away. Because of the severe lack of homogeneity, it is not

possible to write the vertical correlations as a simple depth-time covariance. For any given time-lag, τ , the covariances fall off more rapidly with depth as the acoustic frequency increases. This behavior should be predictable by extending Munk and Zachariessen's formulation to follow the vertical inhomogeneity along two different rays. This complication has yet to be addressed.

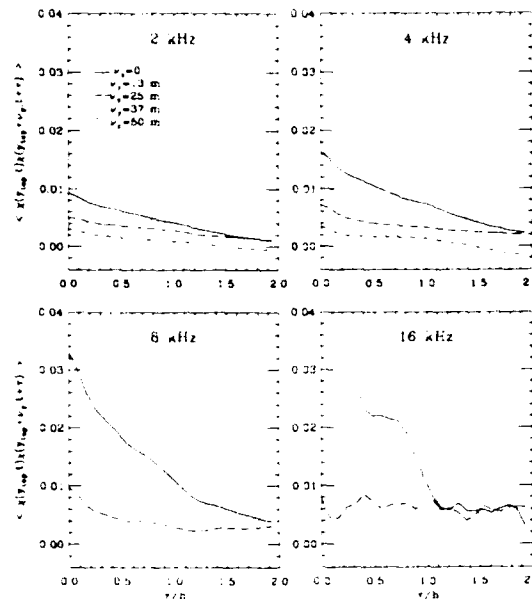


Figure 5. Two-point covariances observed at AATE for depth-separated pairs of log-amplitudes as a function of time lag τ . Depth separations are shown when they are statistically different from zero, $y_{top} = 191$ m.

In summary, the level of acoustic variability measured during AATE was very weak. Rytov approximation theory for acoustic scintillation due to internal waves gives a reasonably good comparison (better than a factor of 2) with the observations. Detailed knowledge of the local environment was required. Our ability to predict the observations is complicated by the vertically inhomogeneous medium, and the lack of stationarity (only 4 days of data could be included in these results). The AATE measurements provide statistics of weak ocean scattering. Comparisons with theory in this regime where the scattering environment is known are surprisingly scarce in the ocean acoustic literature.

4.2. The MATE Lower Path

Unlike the AATE case, pulses traversed this path over a nearly homogeneous scattering environment, and the paths were fixed. The average vertical sound speed profile is shown in Figure 6 along with the two ray paths. The vertical profile of refractive index fluctuations inferred from the internal wave variability is also shown.

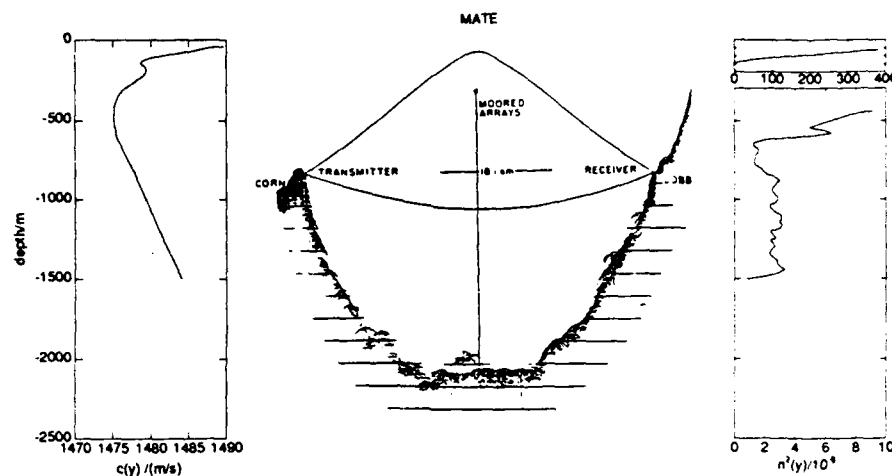


Figure 6. The MATE propagation environment. The location of the moored arrays is shown. The topography of the seamounts is an actual depth-recorder output superimposed on the ray trace. (Note the break in scale at 200 m in the plot of $n^2(y)$).

The validity of the modeled TCF (15) can be demonstrated by comparing the predicted phase spectrum with the observation at a single receiver. Using the results in (3) (neglecting ray curvature effects), the temporal spectrum of acoustic phase at scaled range z_R is given by

$$\Phi_S(\omega) = \langle S^2 \rangle \left[\frac{G_1^{-1}}{\omega^{2.7}} + \frac{b}{2\pi L_p} \frac{4\tau_0}{1 + (\omega\tau_0)^2} \right]; \text{ with } G_1 = \int_f^N \frac{d\omega}{\omega^{2.7}}. \quad (17)$$

The phase variance, $\langle S^2 \rangle$, is obtained using the technique developed by Esswein and Flatte³⁰. (The spectral normalization used here is that the integral over positive frequencies equals the variance. (17) has an additional factor of 2 from (3).) The variance over the upward ray is roughly a factor of 5 greater than that of the downward ray. Figure 7 shows (17) compared to the observations (travel time and phase are interchangeable at MATE). Over the internal wave continuum (between ω_i and ω_b) the comparison is excellent. The lines of energy just above and below ω_i are due to deterministic tides and are not considered here. (Note that the tides are removed in Figure 1.)

We turn our attention to the intensity records. Time gating was used to separate the upward and downward path arrivals. (The instrumentation allowed only one path to be monitored at a time.) The behavior of the intensity time series is very different for the two paths. A portion of the observed intensity series during the time gating change from the downward to the upward path is shown in Figure 8. All four acoustic frequencies are plotted. This figure illustrates the dramatic changes in the intensity probability distributions and the temporal behavior in the various scattering regimes. The normalized intensity variances, $(\langle I^2 \rangle - \langle I \rangle^2) / \langle I \rangle^2$, are listed in Table I. The levels increase

with the acoustic frequency and decrease between 8 and 13 kHz. Predictions for the downward path, obtained using 4th moment theory (Ballard and Uscinski, unpublished) are listed in Table 1. The theory uses the MATE TCF (15), and includes the zeroth order solution plus a correction term. The agreement is excellent.

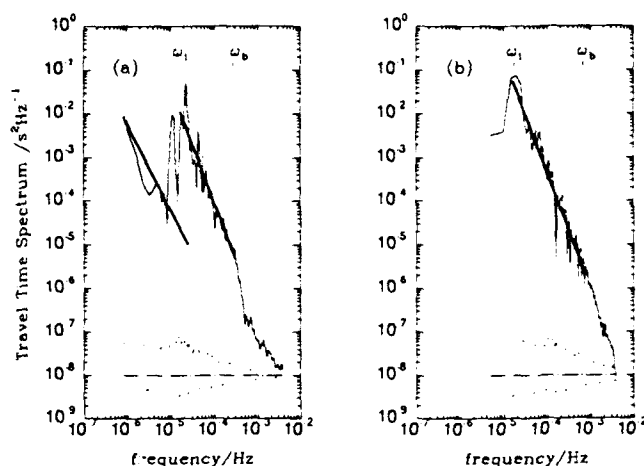


Figure 7. Observed phase spectra compared with the TCF (bold-solid) along the downward (a) and upward paths (b). The finesstructure component, with correlation time-scale $\tau_0 = 500$ h, is seen at frequencies below ω_i in (a). 90% confidence intervals (as in Figure 4) are shown relative to 10^{-8} .

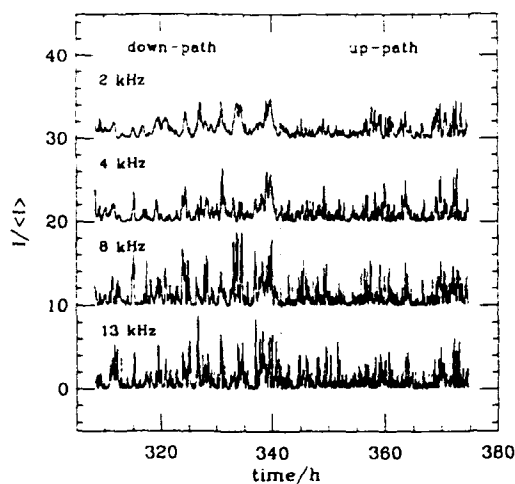


Figure 8. MATE intensities for two inertial periods before and after the instrumentation change from monitoring the downward to the upward path. The time of the change is denoted by a vertical dotted line.

Table I. MATE Observed Intensity Scintillation Indices

Frequencies		2	4	8	13 kHz
Down-Path					
Observed					
Tower 1	(bottom/top)	.71/.64±.08	1.28/1.21±.14	1.48/1.39±.12	1.40/1.34±.10
Tower 2	(bottom/top)	.48/.51±.06	1.07/1.05±.17	1.25/1.23±.14	1.48/1.38±.16
Predicted		.54	1.0	1.5	1.4
Up-Path					
Observed					
Tower 1	(bottom/top)	.65/.68±.07	.90/.97±.12	1.01/1.03±.11	.95/.91±.08
Tower 2	(bottom/top)	.60/.60±.07	.83/.87±.10	1.04/1.14±.11	

The intensity spectra observed at a single receiver are shown in Figure 9 for both the down and the up paths. The zeroth-order fourth moment theory predictions for four scaled ranges for 8 kHz are shown in Figure 10 along with the observed 8 kHz intensity spectrum. The theory and predictions near the inertial frequency are in excellent agreement, and we believe represent the first time that the tail of the Rytov approximation behavior has been observed or predicted in multiple scattering for the ocean TCF.

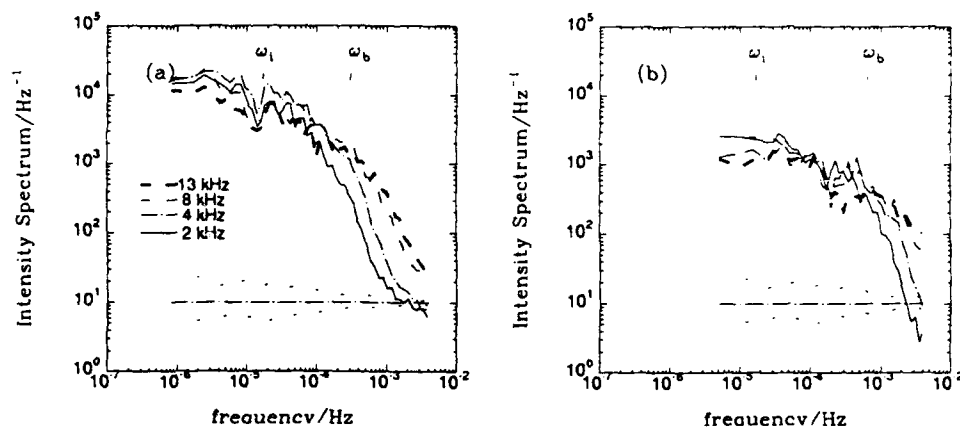


Figure 9. Intensity spectra observed over the MATE downward (a) and upward paths (b). All four acoustic frequencies are over-plotted. For temporal frequencies below 10^{-4} Hz, the spectra are statistically the same. 90% confidence levels as in Figure 4.

Two-frequency and two-point spatial intensity statistics are available from the experiment, but theory evaluation has not been attempted for the extended MATE time series. The 2-point correlations, $\rho_{1,2}(\tau)$, are shown in Figure 11 for vertical (upper graphs) and horizontal (lower graphs) separations. The solid lines are the downward path

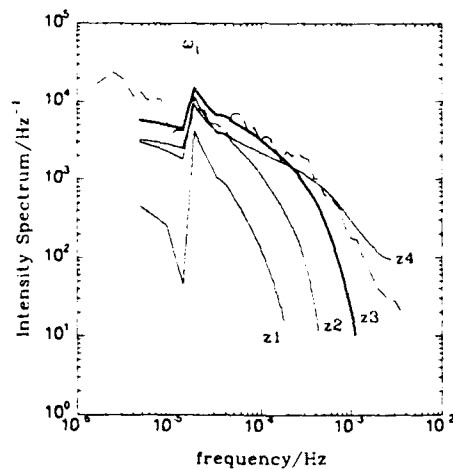


Figure 10. The zeroth-order solution to the moment equation is shown at four scaled ranges. The MATE downward path TCF was used. The observed 8 kHz intensity spectrum (corresponds to scaled range Z3) is over-plotted as dot-dashed.

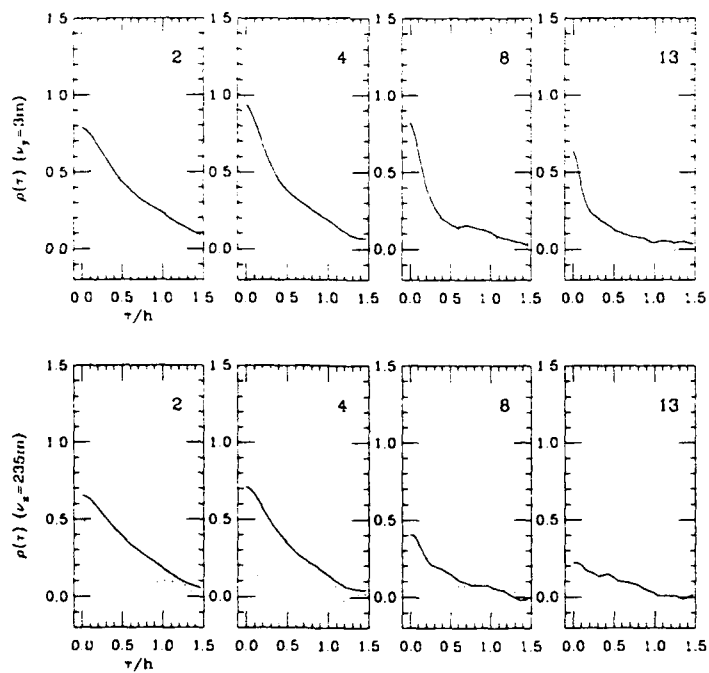


Figure 11. MATE observations of vertical (top) and horizontal (bottom) 2-point intensity correlations as functions of time lag, τ . The downward path results are shown solid and upward path shown dotted for the four acoustic frequencies.

results. The possible pairs of 2-frequency correlations of intensity for the down and up paths are plotted in Figure 12.

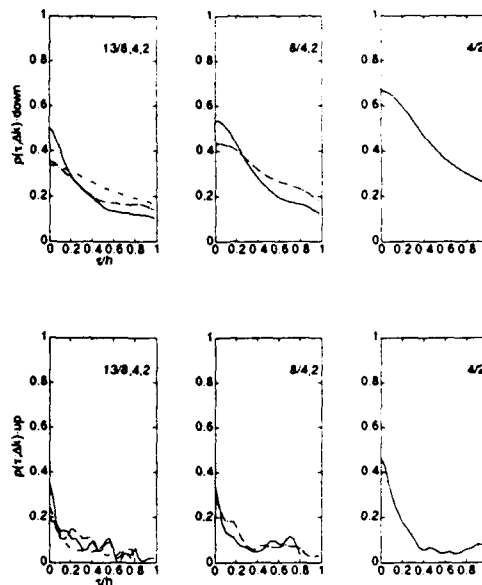


Figure 12. Pairs of 2-frequency correlations of intensity for the down (top) and up (bottom) paths at MATE. The solid, dot-dashed and dashed curves on the left correspond to 13/8, 13/4, and 13/2; solid, dot-dashed in the middle to 8/4, 8/2; and the solid curve on the right to 4/2 respectively.

4.3. The MATE Upper Path

Along the upward directed path at MATE, because $\langle n^2(y) \rangle$ reaches a maximum near the turning point (see Figure 6), the scattering is largely concentrated over the narrow region of the turning point. The scintillation indices and intensity for the upward path are given in Table 1 and Figure 9(b), respectively. Spatial and cross-frequency statistics are shown in Figures 11 and 12. Note that in Figure 9(b) the absence of a roll-off below ω_i may be due to the short duration (2 days) of the time series. In any case, the evaluation of theory for the upper path has yet to be done.

Summarizing MATE, for the four pulse frequencies, on the downward path $\Gamma = (.028 - 7.7) \times 10^4$, $Z = (1.0 - 6.8) \times 10^{-2}$, and on the upward path, $\Gamma = (.20 - 56.) \times 10^4$, and $Z = (.7 - 4.8) \times 10^{-2}$. Observations of the scintillations in the 4 (Γ, Z) regimes for the MATE lower path allowed us to test full range 4th moment theory (autocorrelations) away from the asymptotic regions. The medium correlation functions are messy, but well-tested in an oceanographic sense. Predicting the observed cross-correlations of intensity for spatial and frequency two-point separations awaits further theory development.

5. THE INTENSITY PROBABILITY DISTRIBUTION

We have shown that the intensity variance can be predicted for AATE and MATE, where scattering conditions span wide ranges in Γ and Z . This is a far cry from knowing the full statistics. One might say, "If we knew the two-point correlations of the complex field, the 4th moments of the field, and the intensity probability distributions, we would know a lot about the process." The problems we face in understanding the intensity probability distribution are seen clearly in Figure 13. A one parameter distribution cannot explain the behavior for near to far range, and the true (unknown) distribution has a complicated form. Here we have plotted the 3rd and 4th intensity moments of a plane wave propagating through a medium with a 4th order power law transverse spectrum versus the 2nd moment. $\Gamma = 1000$ (a moderate ocean acoustic propagation value) and the scaled range varied from zero to the point of field saturation ($\langle I^2 \rangle = 2$). The intensity moments of the data (circles) are those computed from many realizations. The fields were generated by Monte-Carlo methods (see Macaskill and Ewart¹⁴ and Ewart¹⁶). Also plotted with various line types are the universal moments of the log normal, K, gamma, Weibull, exponential, and modified exponential³⁴).

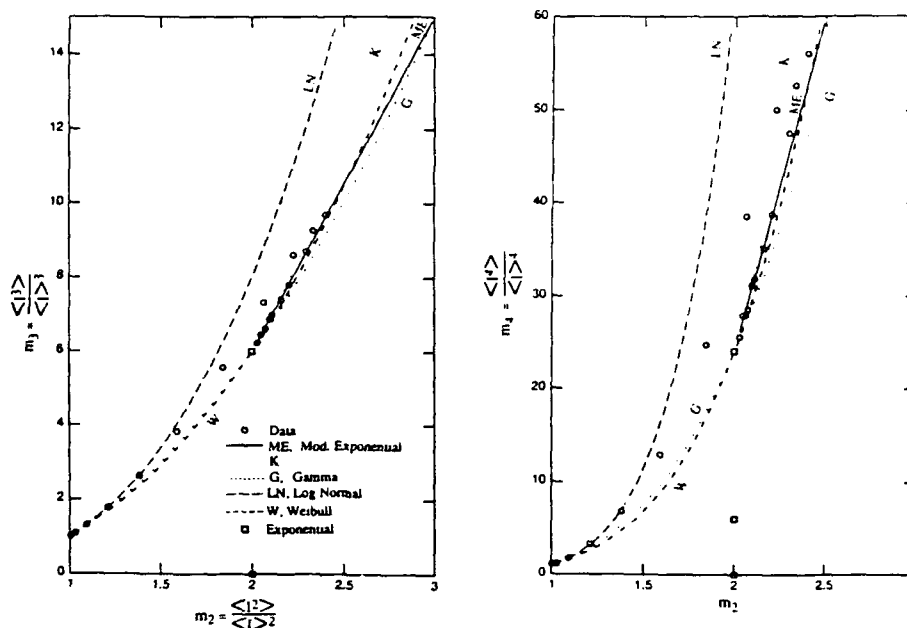


Figure 13. Moments from simulated data that has been fitted by the generalized gamma distribution plotted with several one parameter results defined by m_2 .

The modified exponential distribution is a good fit for the region approaching saturation. The K distribution does not fit this region well, as was shown by Macaskill and Ewart¹⁴. The gamma and Weibull distributions are clearly poor models of the full-range moments. Our point is that the generalized gamma distribution fits all of the data (circles) for all of the (Γ, Z) pairs with a 90% confidence interval acceptance using theoretical-quantile-data-quantile fits for a range of Γ (10^{-1} to 10^7) and Z (10^{-4} to 10^2). Thus, it is not

necessary to use asymptotic forms for the moments or the probability distributions, unless one is considering "first principle" predictions.

In Figure 14 we have plotted contours of the moments $\langle I^2 \rangle / \langle I \rangle^2$, (for the full suite of simulations) as a function of Γ and Z . We see lognormal moments at short ranges, an increase to a peak (the medium focus), and a drop to 2 at longer ranges. Ewart¹⁶ showed that the peak at the medium focus follows closely the prediction of Spivack and Uscinski³⁵. Using numerical solutions to the 4th moment equation, the (Γ, Z) dependence of the peaks, lognormal boundary, and exponential boundary obey the relation, $\Gamma Z^{2.3} = \text{constant}$. It is a relatively simple exercise to generate these results for any other medium TCF. Similar results are available for the 3rd and 4th intensity moments and can be obtained by request.

$$\frac{\langle I^2 \rangle}{\langle I \rangle^2}$$

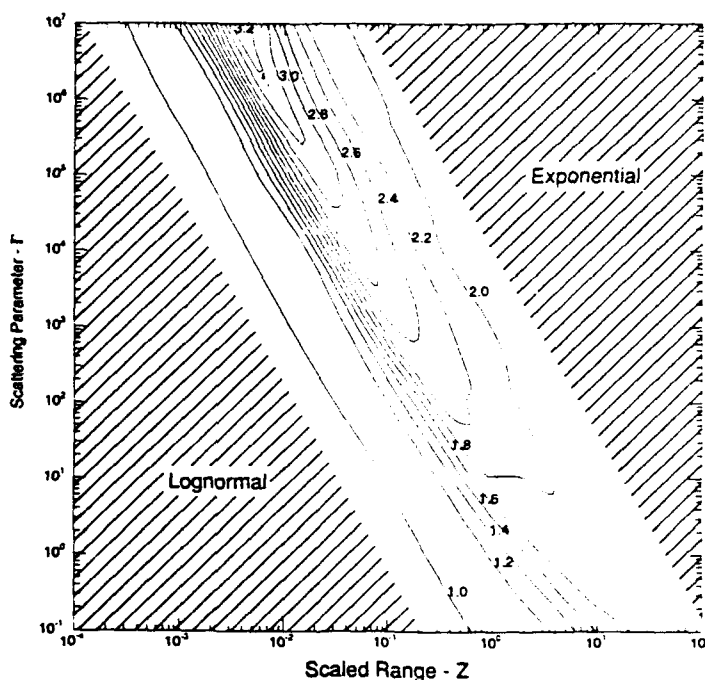


Figure 14. Contours of the 2nd moment from the simulated data.

Ewart and Ballard (unpublished) have completed a similar study for the point source initial condition for a few (Γ, Z) pairs. In this work, the Q-Q fits to the generalized gamma distribution are even better in the region of the medium focus (due to modified sampling techniques), and $\langle I^2 \rangle / \langle I \rangle^2$ is well predicted by moment theory for propagation from a point source. The scintillation indices at the focus increase to higher values at longer ranges for a plane wave as would be expected, but conclusions as to the results of Figure 14 will remain little changed for a point source initial condition. In order to relate these curves to a particular scattering problem, it is only necessary to recognize

that the parameters, $\langle n^2 \rangle L_p$ and L_y are the two parameters of the medium that define Γ and Z . Following Ewart¹⁶, these can be interpreted in terms of k and z_R by inverting (4). Thus, given an assumed medium correlation function and its normalization, it is a simple matter to obtain predictions of observations from the simulated fields.

In the ocean case, the second moment is limited to values below ≈ 3 , due to the strong frequency-dependent chemical absorption. For the same reason, the wavefields do not closely approach saturation.

5.1. MATE and AATE Intensity Probability Distributions

The hypothesis that AATE and MATE intensities are modeled with the generalized gamma distribution is well tested. The MATE data is temporal, and AATE is spatial and temporal. Uscinski and Ballard (unpublished) have modeled the MATE upper path as weak scattering near the point of inflection in the ray at 200 m and a deeply modulated phase screen at the upper turning point. The presence of a deeply modulated screen could indicate that the intensity probability distribution should be Rician; see Roberts³⁶. In Figure 15, upward path intensity moments are plotted on a figure from that paper comparing the Rician normalized intensity moments. The agreement could be taken as support for the phase screen model.

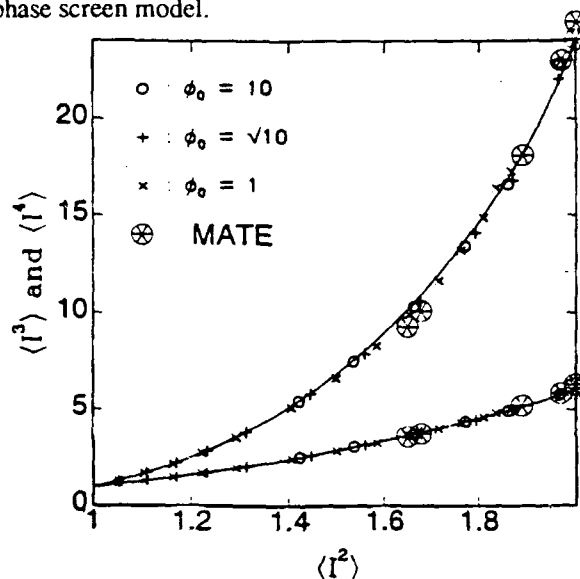


Figure 15. Observed 3rd and 4th intensity moments from the MATE upward path are over-plotted on a figure from Roberts³⁶. The MATE moments are shown as circled asterisks, the other points are those from Roberts's phase screen simulations, and the lines are for the Rician distribution.

6. SUMMARY AND CONCLUSIONS

We have presented results of the predicted and measured intensity correlations for three very different scattering regimes using ocean measurements. A summary of related studies of the intensity probability distribution for both ocean and simulated data has

been included. Our overall conclusion is that the theoretical predictions for the 4th moment of a propagating wavefield have progressed quite far from the asymptotic region theories of a decade ago. Getting the medium TCF correct is an overriding issue, and a difficult one.

Direct 4th moment solvers now being developed will provide predictions that are accurate and relatively easy to compute. As an example, Macaskill and Ballard (unpublished) have achieved predictions superior to those presented in Ewart et al.¹¹ of the MATE cross frequency covariances at $\tau = 0$ using adaptive grid 4th moment solvers. Leonard and Uscinski¹⁷ have successfully predicted cross frequency intensity correlations using adaptive grid 4th moment solvers for simulated data with Gaussian and 4th order power law TCF's up to $\Gamma = 1000$. The solvers are a reasonable approach when one "needs to get an answer," but provide little insight. The 4th moment solutions initiated by Uscinski and Macaskill in the early 1980's are difficult to evaluate for the complex ocean TCF. Clearly, more theoretical work remains. Field and numerical experiment results should be used to test these emerging theories.

6.1. AATE

The phase and intensity for this experiment have been very well predicted using the Rytov approximation theory of Munk and Zachariesen, and the TCF derived from the AIWEX ocean model. The intensity probability distributions from AATE can be modeled with a generalized gamma distribution.

6.2. The MATE Lower Path

The phase auto-spectra are well modeled using Rytov approximation theory and the MATE TCF. The intensity variances are well predicted using 4th moment theory (with zeroth order theory evaluation plus a correction). The auto-spectra of intensity are reasonably well predicted, but improvements are expected when the direct 4th moment solvers are fully tested. Direct solvers are also expected to successfully predict the two-frequency intensity cross spectra. A theoretical issue here is "what was wrong" with the 4th moment theory solutions. The spatial cross spectra have been predicted by Uscinski, but the theory has not been evaluated. The intensity probability distributions for the MATE lower path are well modeled by the generalized gamma distribution.

6.3. The MATE Upper Path

The phase auto-spectra are well modeled using the Rytov approximation theory and the MATE TCF. The sharp turning of the ray inside a horizontal correlation scale at the upper turning point has been modeled as a deeply modulated screen, with small regions of extended media on each side; initial predictions of the intensity variance with that model are not encouraging. The data intensity variance rises to 2, apparently without a peak. A new theory may be required for this case. The intensity moments are fit well using a Rician model (single phase screen assumption). The intensities are also well fit by the generalized gamma distribution; they are not close to exponential, indicating that saturation occurs at a more distant range.

The focus of WPRM studies in the ocean must include the waveguide aspects of the ocean at longer ranges and lower frequencies. A "MATE like" experiment, where the phase and the amplitude are recorded for several frequencies and ranges is needed to make further tests of theory. It is essential that such an experiment include phase and amplitude measurements over a sizable depth range. Regions of the ocean where internal waves dominate the dynamic and passive index of refraction fluctuations are well known, and could be used for such an experiment. Collaboration with many oceanographers would be essential, if one is serious about obtaining the space-time spectrum of the index of refraction and the appropriate TCF. In future intensity probability distribution studies, we will attempt to link the various irradiance distribution models, e.g. I-K distributions, with the generalized gamma model.

7. ACKNOWLEDGMENTS

The authors would like to thank John Ballard, Barry Uscinski, and Charles Macaskill for their assistance and support in preparing this paper. Nina Triffleman edited the manuscript, and Patricia Oakley, and Mike Kenney provided assistance with the computations and plotting. This research was sponsored by the Department of the Navy, Office of the Chief of Naval Research, under Grant N00014-90-J-1260. This article does not necessarily reflect the position or the policy of the Government, and no official endorsement should be inferred.

1. V.I. Shishov, "Theory of wave propagation in random media," *Izvestia VUZ. Radiofizika* 11(6), 866-875 (1968).
2. C. Garrett, and W. Munk, "Space-time scales of internal waves," *Geophys. Fluid Dyn.* 2, 225-264 (1972).
3. B.J. Uscinski, "Parabolic moment equations and acoustic propagation through internal waves," *Proc. R. Soc. Lond. A* 372, 117-148 (1980).
4. T.E. Ewart, "Acoustic fluctuations in the open ocean--a measurement using a fixed refracted path," *J. Acoust. Soc. Am.* 60(1), 46-59 (1976).
5. B.J. Uscinski, "Intensity fluctuations in a multiple scattering medium. Solutions of the fourth moment equation," *Proc. R. Soc. Lond. A* 380, 137-169 (1982).
6. B.J. Uscinski, C. Macaskill and T.E. Ewart, "Intensity fluctuations. Part I: Theory," *J. Acoust. Soc. Am.* 74(5), 1474-1483 (1983).
7. T.E. Ewart, C. Macaskill and B.J. Uscinski, "Intensity fluctuations. Part II: Comparison with the Cobb Experiment," *J. Acoust. Soc. Am.* 74(5), 1484-1499 (1983).
8. C. Macaskill, "An improved solution to the fourth moment equation for intensity fluctuations," *Proc. R. Soc. Lond. A* 386, 461-474 (1983).

-
9. C. Macaskill and T.E. Ewart, "Computer simulation of two-dimensional random wave propagation," *I.M.A. J. of Appl. Math.* **33**, 1-15 (1984).
 10. T.E. Ewart and S. A. Reynolds, "The Mid-Ocean Acoustic Transmission Experiment -MATE-," *J. Acoust. Soc. Am.* **75**(3), 785-802 (1984).
 11. T.E. Ewart, C. Macaskill and B.J. Uscinski, "The MATE acoustic frequency cross correlation of intensity," *J. Acoust. Soc. Am.* **77**(5), 1732-1741 (1985).
 12. B.J. Uscinski and C. Macaskill, "Frequency cross-correlation of intensity fluctuations in multiple scattering," *Optica Acta* **32**(1), 71-89 (1985).
 13. B.J. Uscinski, C. Macaskill and M. Spivack, "Path integrals for wave intensity fluctuations in random media," *J. Sound and Vibration* **106**(3), 509-528 (1986).
 14. C. Macaskill and T.E. Ewart, "The probability distribution of intensity for acoustic propagation in a randomly varying ocean," *J. Acoust. Soc. Am.* **76**(5), 1466-1473 (1984).
 15. T.E. Ewart and D.B. Percival, "Forward scattered waves in random media-the probability distribution of intensity," *J. Acoust. Soc. Am.* **80**(6), 1745-1753 (1986).
 16. T.E. Ewart, "A model of the intensity probability distribution for wave propagation in random media," *J. Acoust. Soc. Am.* **86**(4), 1490-1498 (1989).
 17. S.R. Leonard and B.J. Uscinski, "Accurate numerical solutions for the frequency cross-correlation of intensity fluctuations in a random medium," *App. Opt.* (in press, 1992).
 18. J.M. Martin and S.M. Flatte', "Intensity images and statistics from numerical simulation of wave propagation in 3-D random media," *App. Opt.* **27**(11), 2111-2126 (1988).
 19. J.M. Martin and S.M. Flatte', "Simulation of point-source scintillation through 3-dimensional random media," *J. Opt. Soc. Am.* **7**(5), 838-847 (1990).
 20. Y.J.F. Desaubies, "Acoustic-phase fluctuations induced by internal waves in the ocean," *J. Acoust. Soc. Am.* **60**(4), 795-800 (1976).
 21. Y.J.F. Desaubies, "Analytical representation of internal wave spectra," *J. Phys. Oceanogr.* **6**(6), 976-981 (1976).
 22. Y.J.F. Desaubies, "On the scattering of sound by internal waves in the ocean," *J. Acoust. Soc. Am.* **64**(5), 1460-1469 (1978).
 23. W.H. Munk and F. Zachariasen, "Sound propagation through a fluctuating, stratified ocean: Theory and observation," *J. Acoust. Soc. Am.* **59**(4), 818-838 (1976).

-
24. J.E. Ehrenberg, T.E. Ewart and R.D. Morris, "Signal-processing techniques for resolving individual pulses in a multipath signal," *J. Acoust. Soc. Am.* **63**(6), 1861-1865 (1978).
25. B. Bell, and T.E. Ewart, "Separating multipaths by global optimization of a multidimensional matched filter," *IEEE Trans. Acoust., Spch. Sig. Proc.* **ASSP-34**(5), 1029-1037 (1986).
26. B. Bell and S.A. Reynolds, "A matched filter network for estimating pulse arrival times," *IEEE Trans. Sig. Proc.* **39**(2), 477-481 (1991).
27. T.E. Ewart and S.A. Reynolds, "Instrumentation to measure the depth/time fluctuations in acoustic pulses propagated through arctic internal waves," *J. Atmos. Ocean. Tech.* **7**(1), 129-139 (1990).
28. W.H. Munk, "Internal waves and small-scale processes," in B. Warren and C. Wunsch (Eds.), *Evolution of Physical Oceanography*, MIT Press, Cambridge, MA, 264-291 (1981).
29. M.D. Levine and J.D. Irish, "A statistical description of temperature finestructure in the presence of internal waves," *J. Phys. Oceanogr.* **11**(5), 676-691 (1981).
30. R. Esswein and S.M. Flatte, "Calculation of the strength and diffraction parameters in oceanic sound transmission," *J. Acoust. Soc. Am.* **67**(5), 1523-1531 (1980).
31. A. Ishimaru, *Wave Propagation and Scattering in Random Media Vol. 2*, Academic Press, New York, 389-390 (1978).
32. M.D. Levine, "Internal waves under the arctic ice pack during AIWEX: The coherence structure," *J. Geophys. Res.* **95**(C5), 7347-7357 (1990).
33. M.D. Levine, J.D. Irish, T.E. Ewart and S.A. Reynolds, "Simultaneous spatial and temporal measurements of the internal wave field during MATE," *J. Geophys. Res.* **91**(C8), 9709-9719 (1986).
34. K.S. Gochelashvili and V.I. Shishov, "Strong fluctuations of laser radiation intensity in a turbulent atmosphere-- the distribution function," *Sov. Phys. JETP* **47**(6), 1028-1030 (1978).
35. M. Spivack and B.J. Uscinski, "Accurate numerical solution of the fourth-moment equation for very large values of Γ ," *J. Mod. Opt.* **35**(11), 1741-1755 (1988).
36. D.L. Roberts, "The probability distribution of intensity fluctuations due to a random phase screen with an exponential autocorrelation function," in B.J. Uscinski (Ed.), *Wave Propagation and Scattering*, Clarendon Press, Oxford, UK, 129-154 (1986).